Waveguide-integrated niobium- nitride detectors for on-chip quantum nanophotonics

IOP Publishing Nanotechnology
Nanotechnology 32 (2021) 104001 (9pp) https://doi.org/10.1088/1361-6528/abcc97

Waveguide-integrated niobium- nitride detectors for on-chip quantum nanophotonics

Francesco Mattioli, Sara Cibella, Alessandro Gaggero, Francesco Martini and Roberto Leoni

Istituto di Fotonica e Nanotecnologie - CNR, Via Cineto Romano 42, I-00156 Roma, Italy

E-mail: francesco.mattioli@ifn.cnr.it

Received 3 October 2020, revised 4 November 2020
Accepted for publication 20 November 2020
Published 10 December 2020

Abstract

NbN-based detectors can detect light from the granular regime (single or few photons) up to weak continuous photon fluxes at wavelengths ranging from visible light up to mid-IR. The article reports our recent results on a novel linear detector, the waveguide-integrated hot electron bolometer (HEB) capable to measure photon fluxes of large coherent beams in a regime in which superconducting nanowire single photon detectors (SNSPDs) are not efficient due to their strong nonlinearity. SNSPDs, photon number resolving detectors and amplitude multiplexing readout schemes, all integrated on photonic circuits are also discussed in the paper. The compatibility of the integrated HEB detectors with the SNSPDs technology can allow the characterization of complex non classical states of light within the same chip.

Keywords: superconducting nanowires single photon detectors, hot electron bolometers, waveguides, photonic integrated circuits

(Some figures may appear in colour only in the online journal)

1. Introduction

The implementation of practical quantum information technologies for communication [1], computation [2] and simulation [3] based on photons faces a fast increasing level of complexity from the hardware point of view. Bulk optical elements mounted onto optical benches are not suited for large-scale experiments as they are plagued by inherent instability. In the past 10 years, many efforts have been devoted to develop an integrated platform containing all functionalities needed by quantum-information experiments with photons. Three main functionalities need to be integrated on the same platform [4]: quantum-state sources, linear-optic circuits and detectors. Several experiments have been performed or proposed that exploit photonic integrated circuits (PICs), including boson sampling, quantum walk, and quantum simulation [5–9] but with hybrid setups, i.e. not integrating directly on-chip sources and detectors, being the latter externally fiber-coupled to the PICs.

In the telecom spectral range, the superconducting nanowire single photon detector (SNSPD) [10, 11] is the only technology that showed on-chip integration feasibility with confined waveguides [12–19] together with outstanding performance in terms of detection efficiency, dark count rate, and timing resolution. Since their first implementation [10], several experiments have exploited nanostructured niobium nitride (NbN) superconducting films demonstrating their capability to detect light in the granular regime from single photons up to few photon fluxes. Thanks to the intrinsic nonlinerity of the detection mechanism of SNSPDs, the implementation of the spatial-multiplexing [20, 21] is particularly suitable for achieving photon number resolution. However, due to their strong nonlinearity, SNSPDs are not suited to measure photon fluxes of large coherent beams. To overcome this limitation here we report our recent results on a novel linear detector, the waveguide-integrated hot-electron bolometer (HEB). In this case, the detector based on a small ultrathin NbN layer and coupled to a ridge-waveguide, exploits the hot electron mechanism in a metal [22], and can

have a noise equivalent power (NEP) limited by the shot-noise of the photon source [23]. The compatibility of the integrated HEB detectors with the SNSPDs technology can allow the characterization of complex non classical states of light within the same chip.

In this paper, we describe some results on the integration of NbN ultrathin films nanostructured in such a way to obtain SNSPDs, array of SNSPDs and HEBs integrated with photonic circuits. In section 2, the optical properties of NbN films as active material for light detection are highlighted. In section 3, the SNSPD working principle is described together with the spatial multiplexing required to achieve the photon number resolution and for encoding the position of a photon detection event in an array of SNSPDs. Finally, in section 4, integrated HEBs are introduced together with their low temperature characterization at 1550 nm wavelength.

2. Ultrathin NbN as active materials

Ultrathin NbN films (typically 4–6 nm) remain superconducting even if structured into nanostrips or small slab with a critical temperature of 10–12 K (with a transition width <1 K) allowing in this way the efficient detection of photons. The NbN_x exists in different crystal structures depending on its stoichiometry. In particular, the phase with the face centered cubic (fcc) structure (δ-NbN) shows the highest critical (or transition) temperature T_C.

The NbN film is generally deposited by dc-magnetron reactive sputtering in an Ar + N_2 ambient. Deposition conditions influence both the stoichiometry and the morphology of the film determining consequently both the crystal phase and the lattice parameters that strongly affect the superconducting properties of NbN films. The Nb/N ratio in the film is the main parameter that needs to be optimized together with the total pressure P_{tot} and the deposition bias current I_c (typically, $I_c = 250$ mA, $P_{tot} = 2$ mBar and 22% N_2 in the Ar + N_2 mixture) to improve the film quality (grain size and island structure). Other important parameters are the substrate temperature and the substrate of choice: for both SOI and Si_3N_4 wafers the substrate is heated at ~750 °C. Differently, a lower deposition temperature of about 350 °C is used to deposit NbN on GaAs substrates to avoid As evaporation and to prevent a poor surface morphology. In fact a substrate roughness of the same order of magnitude of the film thickness deplects the superconducting properties of the film [24].

Other superconducting materials have been explored as photosensitive material for single photon detectors such as NbTiN, TaN, NbSi and amorphous WSi, MoSi and MoGe [25]. Differently from NbN, amorphous films have a smaller superconducting energy gap, hence, an operating temperature lower than 1 K. A smaller energy gap allows saturated detection efficiency, but also lower critical density current (hence a reduced signal-to-noise ratio (SNR)) and larger timing jitter if compared to NbN films. For this reason, the use of NbN as a photon-absorbing material remains appealing. Moreover, its high transition temperature allows to operate detectors efficiently in the 2–3 K temperature range, easily reachable with compact cryogen free GM refrigerators. NbN nanowires show high critical current and fast photoresponsive properties [10] with an electron–electron interaction time of 6.5 ps, an electron–phonon interaction time τ_{e-p} of 11.6 ps and a phonon escape time on sapphire substrates τ_{es} of 21 ps at 2.15 K [26].

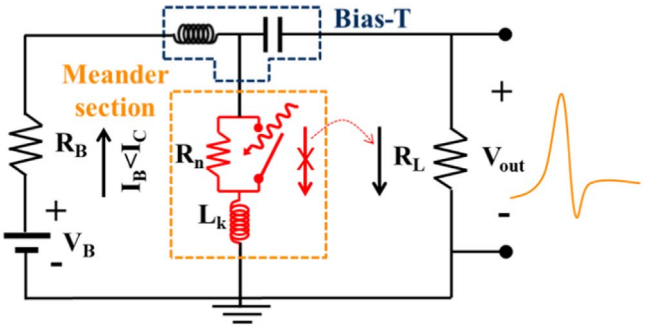

Figure 1. Bias and readout equivalent circuits of an SNSPD. The superconducting nanowire is schematized as a superconducting switch (switch 'closed' means superconducting state) in parallel with its normal resistance R_n and in series with the kinetic inductance L_k. R_L is the load resistance of the read out electronics. When a photon is absorbed, the switch opens and the bias current is diverted in the readout resistance R_L giving rise to a voltage pulse of amplitude $V_{out} \approx I_B R_L$.

3. Superconducting nanowire single photon detectors

3.1. SNSPDs working principle

. Although different models [27–29] and several experiments [30–34] have been proposed to describe accurately the detection mechanism of superconducting nanowires, a definitive model is still missing. One common model of the detection mechanism can be summarized as follow. The absorption of a single photon in the nanowire generates a cloud of $N_q \approx$ 500–1000 quasiparticles ($N_q \approx h\nu/\Delta$, where $h\nu$ is the photon energy and Δ is the superconductor energy gap). The quasiparticles cloud causes locally a suppression of the superconducting properties of the material and induces a redistribution of the supercurrent towards the nanowire sidewalls. In this condition, due to the lowering of the potential barrier, magnetic vortices can enter the nanowire promoting the transition to the normal state of the complete section of the nanowire. Once the whole section of the nanowire is in the normal state, the bias current is diverted to the external read out circuit (switch opens in figure 1), as the local resistance $R_n \sim 1$ kΩ is much larger than the load resistance $R_L \sim 50$ Ω of the readout circuit. Consequently, a fast rise (<100 ps) of the output voltage V_{out} is produced. However, in this condition the nanowire is no longer current biased and then it rapidly cools down again in the superconducting state allowing the restoring (switch in figure 1 closes again) of the bias current. With this mechanism the output voltage exponentially decreases to zero with a time constant L_k/R_L (where L_k is the kinetic

inductance of the superconducting nanowire that is of the order of 50–100 pH/□ for NbN) resetting the detector for registering a new photon. Due to this mechanism, the voltage pulse amplitude is $V_{out} \approx I_B R_L$ and only weakly dependent on the resistance of the hotspot R_n generated by the photon absorption, so single and few-photon absorption give rise to pulses nearly of the same height.

3.1.1. SNSPD fabrication process. Once the superconducting material deposition is done, several steps of electron beam lithography (EBL) are required to fabricate the whole detector. The first step defines, by lift off on PMMA, the pads together with the markers needed to align the successive lithography steps. Ti/Au pads are generally designed as a 50 Ω coplanar waveguide to minimize the reflections of the fast output signals. The nanowire (typical width ⩽100 nm) is lithographically defined on a negative-tone, 180 nm thick electronic resist (hydrogen silsesquioxane —HSQ). The pattern obtained on the HSQ mask is then transferred on the NbN film using a reactive ion etching (RIE) process based on a CHF_3/SF_6 gas mixture. In this way, all the unwanted material uncovered with the HSQ or the Ti/Au pads is removed. The nanowire patterning is critical as the nanowire width uniformity can significantly affect the detection efficiency [35]. In fact, the presence of just a single defect can reduce the critical current of the detector [36], forcing most of the SNSPD to be biased with a current lower than the optimal one, reducing drastically the detection efficiency.

3.2. Waveguide-integrated SNSPDs

The system detection efficiency (SDE), defined as the probability that a photon in the optical fiber will result in a detectable electrical pulse, can be factorized in three independent efficiencies η_a, η_i and η_c where η_a identifies the optical absorption, η_i the internal efficiency and η_c the coupling efficiency. SNSPDs are usually coupled with the optical mode of a single mode fiber with a top/bottom illumination configuration and are embedded in an optical cavity in order to enhance the absorption probability [24]. In 2011 however, the first demonstration of an SNSPD integrated with a photonic circuit has been reported [12]. In this case, the NbN nanowires are coupled to the evanescent field of the optical mode travelling in a 1.85 μm wide GaAs waveguide (see figure 2(a)). In this first attempt, the waveguide was designed to propagate only the TE mode of the light. Using this approach the length of the nanowires can be tuned to increase the absorption probability up to 100% with a reduced length of the nanowires if compared to top-illuminated detectors [12].

The waveguide-integrated SNSPD was tested by end-fire coupled light ($\lambda = 1300$ nm) by using a polarization-maintaining lensed fiber (producing a spot with nominal diameter of 2.5 ± 0.5 μm) close to the waveguide end. The sample was mounted on the cold finger of a continuous flow helium cryostat.

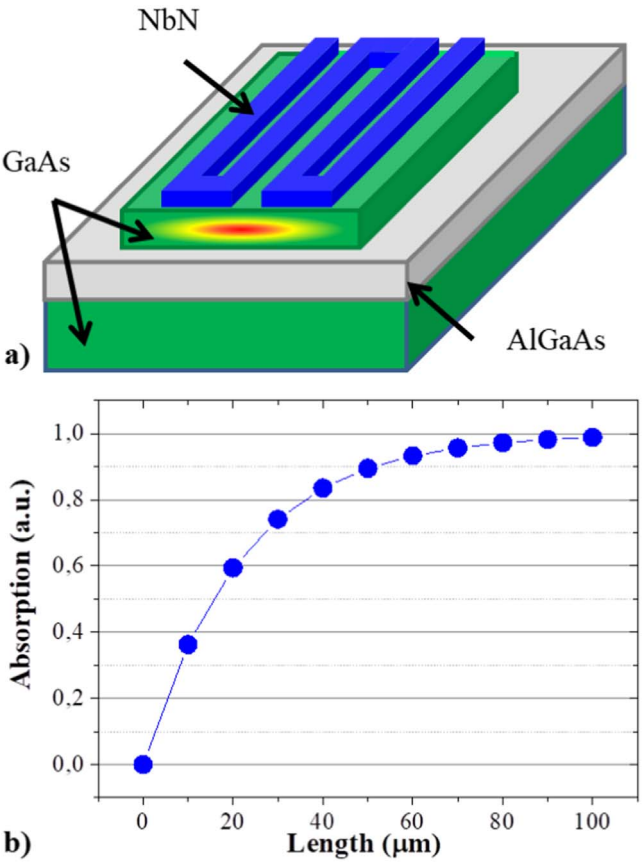

Figure 2. (a) Schematic view of the SNSPD integrated on a GaAs waveguide [12]; (b) absorption of 100 nm wide NbN nanowires ($\lambda = 1300$ nm) as a function of the nanowire length. This plot has been obtained considering a modal absorption coefficient $\alpha_{abs} = 451$ cm.

The 50 μm long length of the SNSPD showed a SDE = 3.4% and a on-chip detection efficiency, DE = $\eta_a \eta_i \approx 20\%$ for the TE polarization at 1300 nm, with a timing resolution of 60 ps and a dead times of few ns.

3.3. Beyond single photon detection with spatial multiplexing

To overcome the intrinsic nonlinear response of SNSPDs to the number of incident photons, several groups have proposed different approaches ranging from time multiplexing schemes [37, 38] or spatial multiplexing using a multi-element scheme [39] to achieve photon number resolution. However, the most promising architectures are obtained when the electrical circuit is designed so that the photon number information is encoded into a single output pulse [40]. In this way, the complexity of the read-out electronics is minimized, allowing the scaling to larger photon numbers. The implementation of a single read-out that sums up the signals coming from the different array elements (pixels) in a single output pulse allows the realization of a fast, photon-number-resolving (PNR) detector with a high dynamic range.

In order to sum up the signals coming from the array elements in a single output and scale up with the photon number at the same time, the series nanowire detector, SND, was proposed [41]. In the SND configuration each nanowire

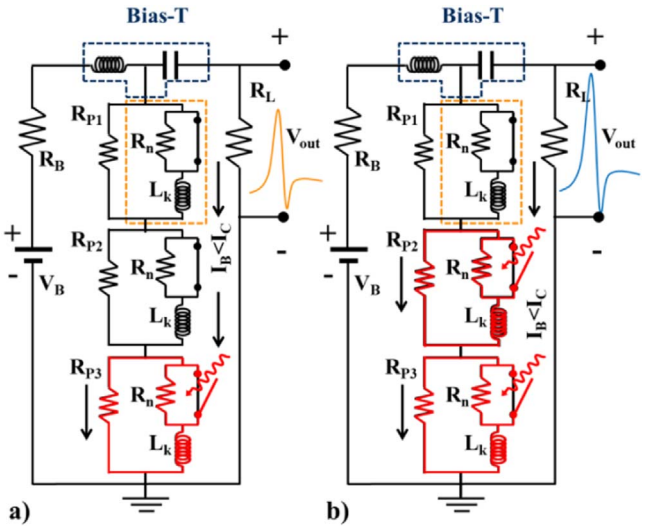

Figure 3. Electrical equivalent circuit of a SND consisting in a three-pixel PNR detector. Each superconducting nanowire pixel, schematized as a superconducting switch in parallel with its normal resistance and in series with the kinetic inductance L_k (orange box in the first pixel), is connected in parallel with a resistance R_{pi} fabricated on-chip. When a photon is absorbed (red lower pixel in (a)) the switch opens and the bias current I_b is diverted into the parallel resistance R_{pi} and a voltage pulse is generated at the output. (b) If more pixels absorbs a photon, the voltage pulses sum up at the output.

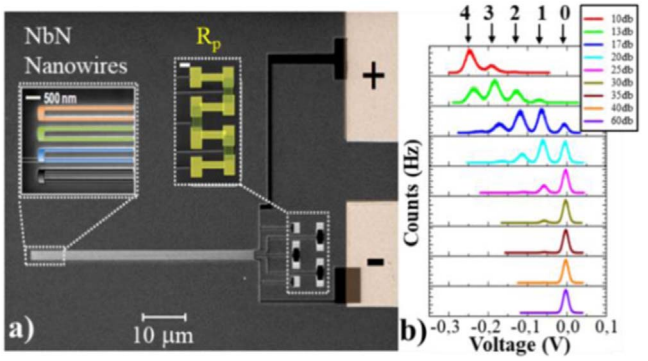

Figure 4. (a) Scanning electron microscope image of the SND on top of GaAs waveguide. Inset on the upper left: a blow-up image of the 100 nm wide NbN four wires (the wires have been colored for clarity). Inset on the upper right: a close-up, false-colored image of four AuPd parallel resistances (the scale bar of both the insets is 500 nm). (b) Histograms of the pulse heights for different optical power attenuations of a pulsed laser down to the few and single photon level. Arrows on top indicate the mean number of photons absorbed. Reprinted from [15], with the permission of AIP Publishing.

element/pixel is connected to a parallel resistor ($R_{p1} = R_{pn} = R_p$), integrated on the chip together with the nanowires (see figure 3). All the pixels are in series so that they are equally biased with the same bias current I_b.

When the detector is not illuminated, each pixel is in the superconducting state and the I_b flows through the nanowire. The value of each R_p is much lower than the normal resistance of the nanowire $R_n(t)$. In this condition, when a photon is absorbed in a pixel, the bias current in that pixel is diverted into the parallel resistor (if $R_L \gg R_p$), generating in this way a voltage pulse (figure 3(a)). If more pixels absorb a photon, the bias current flows into the corresponding parallel resistors. In this way, the voltages produced across each R_p add up at the output. Hence, the pulse height is proportional to the number of firing pixels and hence to the number of absorbed photons (figure 3(b)). In any spatial multiplexed PNR detector, the absorption of two or more photons in the same pixel introduces an error in the photon number measurement affecting the detector fidelity. Due to this effect, the detector is linear only up to a number of photons that is lower than the number of its pixels. This limit can however be estimated and the error can be minimized using a number of pixels large enough with respect to the maximum number of photons to be detected in the experiment.

In the case of the usual readout via a coaxial cable extending from the low temperature detector to the room temperature amplifier, once one pixel absorbs the photon the bias current is partially redistributed also to the load, temporarily reducing the bias in the unfiring branches. This effect, leads to an increase of the dead time together with a reduction of the output voltage and hence of the linearity of the detector. This drawback can be minimized by using a preamplifier with large input impedance placed in the cryostat close to the SND.

The SND approach has been experimentally demonstrated up to 24 photons [20, 42, 43] allowing in this way the realization of a fast and high dynamic range PNR detector with a single readout line simplifying the readout complexity if compared with other approaches.

3.3.1. Integrated photon number resolving detectors. The first attempt to integrate a SND in a PIC was performed in 2013 on a GaAs ridge waveguides [15]. The SND has four NbN nanowires connected in series and each one has a parallel on-chip resistance. The SND was fabricated on top of a 3.85 μm wide and 350 nm thick ridge GaAs/AlGaAs waveguide, etched by 260 nm on top of $Al_{0.75}Ga_{0.25}As$ cladding layer (figure 4(a)). A continuous-wave laser attenuated to the single photon level ($\lambda = 1310$ nm) was fiber-end coupled to the waveguide to characterize optically the SND. The on-chip DE reaches 24% for TE and 22% for TM polarization ($I_b = 9.3$ μA). The PNR capability was tested using an attenuated pulsed diode laser ($\approx$100 ps pulse width, 2 MHz repetition rate) to probe the Poissonian statistics at the few photon regime: distinct detection peaks that correspond to the detection of 0–4 photons are well separated one from the other (see figure 4(b)).

3.3.2. Integrated amplitude multiplexing readout. The complexity of PIC architectures for state of the art quantum optics experiments requires the integration of several tens of SNSPDs. The use of dedicated readout electronics for each detector channel is not only unpractical, but has also a strong impact on the thermal budget allowed by cryostats used for the experiments.

Even though several multiplexing schemes able to encode the position of the absorbed photons in the signal response have been proposed [44–48], the capability to read

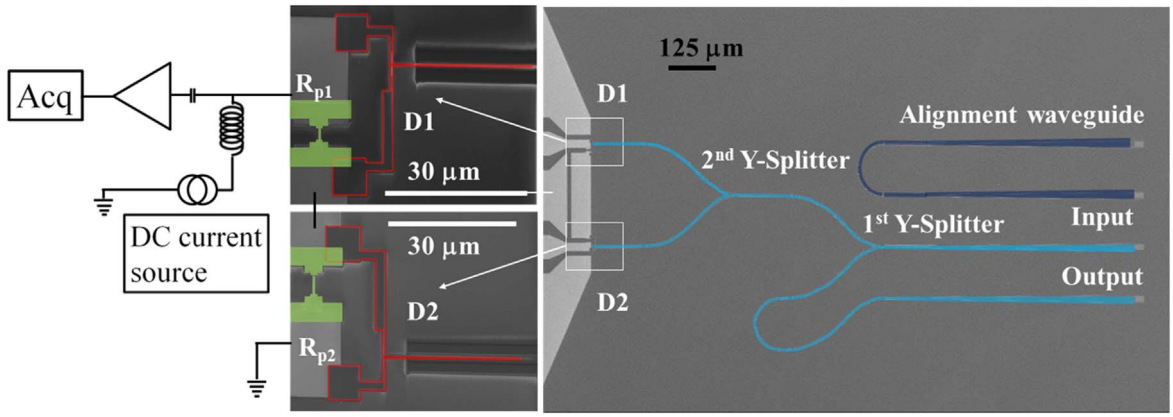

Figure 5. The Optical Society. Scanning electron micrograph of the SNSPD array consisting of two detectors (D1 and D2) integrated on top of a (Si_3N_4) PIC made of two 50:50 Y splitters. Input/output ports are realized with grating couplers. The enlarged views of D1 and D2 show in green the parallel resistances R_{p1} and R_{p2} of different lengths and hence different values. Reprinted with permission from [21] © The Optical Society.

out multiple SNSPDs with only one coaxial cable and without the requirement of complex post processing of the signal is highly desirable.

Recently, it has been proposed the amplitude-multiplexing scheme [21] that has similarities with the photon number resolving architectures (SND) described in the previous section, but expands such functionality thanks to the capability to discriminate the position where the photon is absorbed, characteristic of paramount importance in quantum integrated photonics applications. As in the SND approach, each of the N active elements of the array has an on-chip AuPd resistor R_{pi} in parallel (by design the nanowire normal resistance R_n is $\gg R_{pi}$, see figure 3) but this time the value of each R_{pi} is different with the respect to the each other. Once a detector/pixel absorbs a photon (for example the m^{th}), the bias current is diverted into the corresponding parallel resistance R_{pm}, giving rise to a voltage pulse $V_{out} = I_b R_{pm}||R_L$. The position of the photon-absorption event is then encoded in the pulse amplitude, which changes depending on where the absorption takes place.

The proof of concept reported on [21] is based on a two-element array integrated in a silicon nitride (Si_3N_4) PIC. Two detectors, D1 and D2 have been connected in series and each of them is in parallel with an on-chip resistance, R_{p1} and R_{p2}, where $R_{p2} = 2\ R_{p1}$(figure 5). The NbN absorption region of the nanowire has been chosen to be 30 μm long, ensuring a good photon absorption probability, up to 77% at the wavelength $\lambda = 1550$ nm. A fast and reliable light coupling between external optical fibers and the PIC has been obtained by means of a fiber array aligned at room temperature to the ports of the PIC (each one made with a grating coupler) and then glued to the chip. The readout electronics consists of two bias tees and two room temperature RF amplifiers in series with a total gain of 49 dB and a frequency bandwidth 0.1–500 MHz.

The travelling photons at $\lambda = 1550$ nm wavelength, are generated by a 10 ps pulsed laser and injected through the input port of the PIC. Figure 6(a) shows the count rate as a function of the trigger level taken for different bias currents of

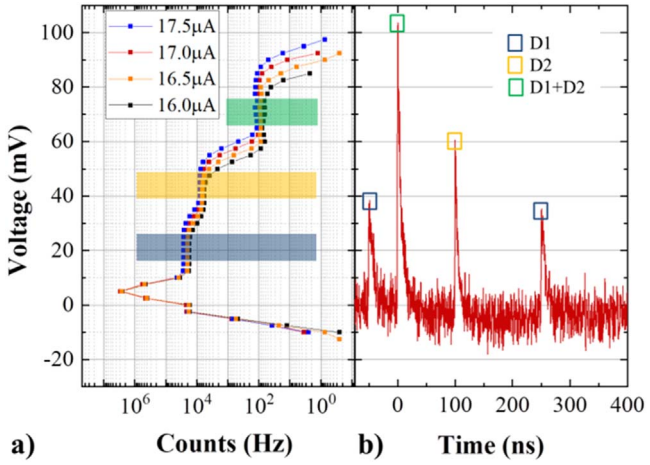

Figure 6. (a) Count rate versus trigger level (TL) for different I_b of the detector (17.5 μA blue curve, 17.0 μA red curve, 16.5 μA orange curve and 16.0 μA black curve). The graph has been rotated 90° counter clockwise in order to align the TL voltage with the Y axis (voltage) of the graph in (b). (b) Output signal recording ($I_b = 17.0$ μA) taken from the oscilloscope. Peaks with three different heights are visible.

the detector ($I_b = 17.5$ μA, 17.0 μA, 16.5 μA and 16.0 μA) with an average photon number per pulse $\langle\mu\rangle = 1$ to increase the probability of a coincidence event that otherwise would be too low in the single photon regime. In all those cases, three plateaus are clearly visible. The first plateau level (10–30 mV) includes the counts due to D1 (pulses with the lowest amplitude), D2 and those due to the coincidences coming from the simultaneous firing of both D1 and D2. The second plateau (35–50 mV) takes into account pulses coming from D2 and from the simultaneous firing of the two detectors, while the third plateau (from 65 to 80 mV) is due only to the coincidence events. In the range from −10 to 10 mV the electronic noise dominates the curve (this part can be removed subtracting the dark counts curve from each count curve). The three firing events (D1-blue squares, D2-orange squares and the simultaneous firing of D1 and D2-green

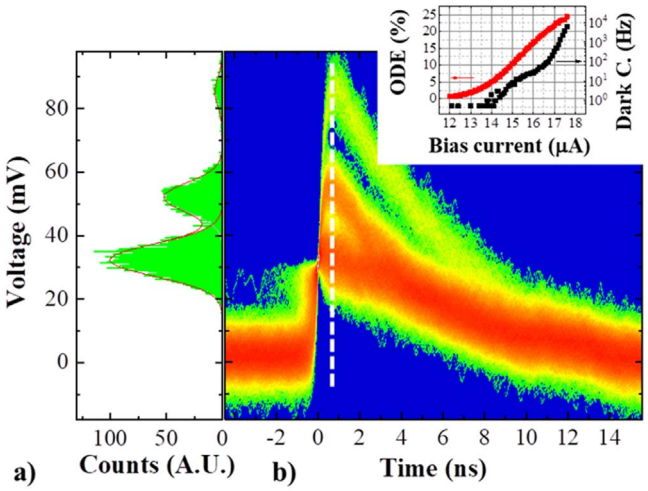

Figure 7. (b) Persistence traces of the output pulses of the array of detectors D1 and D2 taken from the oscilloscope. (a) Histogram of the voltage levels taken in a small time interval at $\Delta t = 700$ ps of the persistency maps (white vertical dashed line of figure 7(b)). Inset: on-chip detection efficiency (ODE) and dark counts rate (DCR) of the whole device. Average photon number per pulse $\langle \mu \rangle = 0.1$.

squares) are clearly visible also in the output signal trace taken from the oscilloscope (figure 6(b)).

From the persistency traces of the output pulses (see figure 7(b)) it is possible to obtain the histograms of the voltage pulse heights (figure 7(a)) for $\langle \mu \rangle = 1$. The histograms are taken in a short time interval $\Delta t = 700$ ps, close to the pulse peak. With a Gaussian fit, the three peak positions and their FWHM values can be retrieved and consequently the values of the resistance $R_{p1} = 7.81\ \Omega$ and $R_{p2} = 14.98\ \Omega$ can be inferred. These values are in good agreement with the expected values of R_{p1} and $R_{p2} \approx 2\ R_{p1}$.

The amplitude-multiplexing read out scheme is particularly suited for the implementation of complex single photon experiments in which several optical modes must be read out simultaneously. In this case, the main figure of merit is the number of channels that can be distinguished with a single output line. As discussed in [21], the scalability of the amplitude multiplexing approach depends on the input resistance of the readout electronics R_{out}, that generally coincides with the RF amplifier impedance, and the SNR. Using a room amplifier (LNA), up to 30 channels can be read using a single read out in the single photon regime. Reducing the noise temperature of the amplifier (for example using a cryogenic amplifier) the number of channels can be furtherly increased. The main advantage of this multiplexing scheme is its compatibility with single coaxial line standard readout electronics: moreover it is possible to implement this scheme with other multiplexing schemes [45] allowing to reach even higher channels number.

4. Waveguide integrated hot electron bolometers

The SNSPD response, being strongly nonlinear, is not well suited to measure photon fluxes of large coherent beams. Even though this effect can be mitigated with PNR architectures, it could be desirable to measure linearly larger light powers with a technology compatible with both cryogenic temperatures and photonic materials. Exploiting the caracteristichs of the NbN ultrathin films, a class of linear detectors can be obtained by integrating a superconducting HEB in a PIC. The electrical resistance in ultrathin (4–7 nm) NbN films depends on the electron temperature. In fact, NbN ultrathin films have a very high scattering rate due to surface effect and hence a short electron mean free path, which is in the range $l = 1$–10 nm. In these films, it is found that the electron-electron interaction is enhanced resulting in a short interaction time (7 ps, being proportional to l) while the electron–phonon interaction is weakened (being proportional to l^{-1}). Consequently, the electrons can reach thermal equilibrium at a temperature different from the lattice temperature [49]. For this reason, when a HEB, i.e. a small NbN slab, absorbs light power, the electrons reach a temperature higher than the lattice temperature, making the HEB a detector very sensitive to low photon fluxes. Due to their large sensitivity and speed, HEBs have been the preferred choice for detecting light from near-infrared [50] and mid-infrared [51], up to THz spectral range [52, 53].

Recently, HEBs have been integrated on top of a SOI photonic circuit using a procedure similar to that used for the fabrication of SNSPDs [23]. As opposed to [23], where the HEB is used as a mixer (i.e. photons are directly used to heat the electrons to the operating point), here we report the performances of a HEB operated in a direct mode, where a heater is placed underneath the sample to heat both the electron and phonon temperature to the desired operating point.

The HEB consists of a thin layer of NbN (6 nm) deposited by reactive dc magnetron sputtering on top of standard 220 nm-thick SOI wafer (BOX thickness 2 μm). The sensitive area of the HEB, the contact pads and Si photonic layers are all defined by means of EBL, lift off techniques and RIE etching steps. The light propagating in the SOI waveguide is halved by a Y-splitter and one of the two ports (input) is used to feed light to the HEB (in this case with a $3 \times 3\ \mu m^2$ active area) meanwhile the other port (output) is employed for monitoring the coupled light (see figure 8(a)). The measurements are performed at temperatures close to the critical temperature ($\sim$9 K) of the NbN (inset of figure 8(b)). To operate the HEB in this regime, the chip is mounted on a GM closed-cycle refrigerator and cooled down to its base temperature. The light coupling at cryogenic temperature is obtained using the same gluing procedure described in section 3.3.2. The light coming from a telecom laser is injected through the input port of the fiber array and coupled inside the PIC thanks to a grating coupler. A RF sinusoidal signal (10 MHz) is applied to a CW-laser to modulate the light signal ($\lambda = 1550$ nm). A bias tee was used to both bias the detector with a DC current generator and to extract the RF signal. The RF signal, amplified with a cryogenic low noise

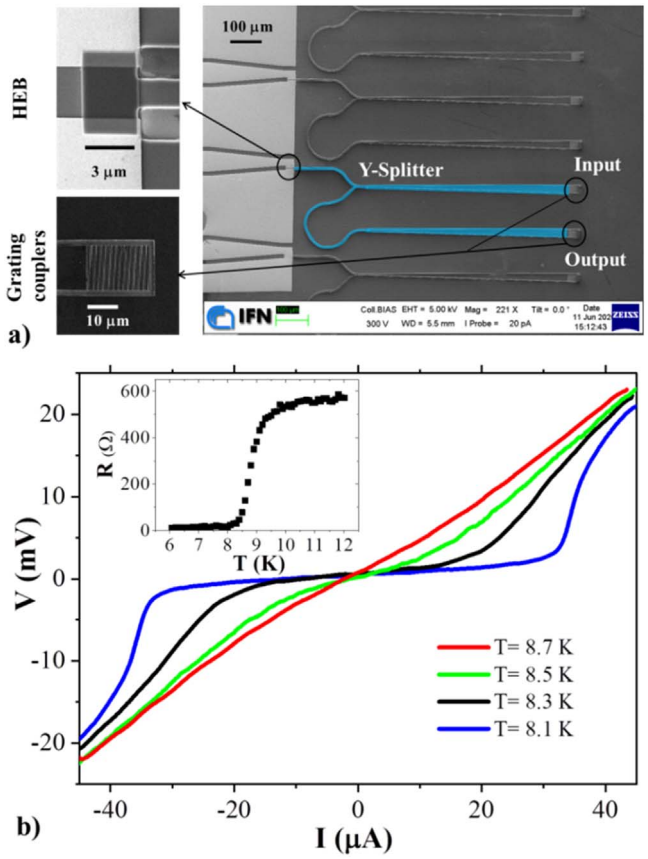

Figure 8. (a) SEM images of the Si PIC coupled to a 3 × 3 μm^2 active area HEB. The SOI waveguide is halved by a Y-splitter and one of the two ports (each one made with a grating coupler) is used to feed light to the HEB. (b) *IV* characteristics of the HEB taken at different temperatures. Inset: resistance-temperature curve of the fabricated HEB.

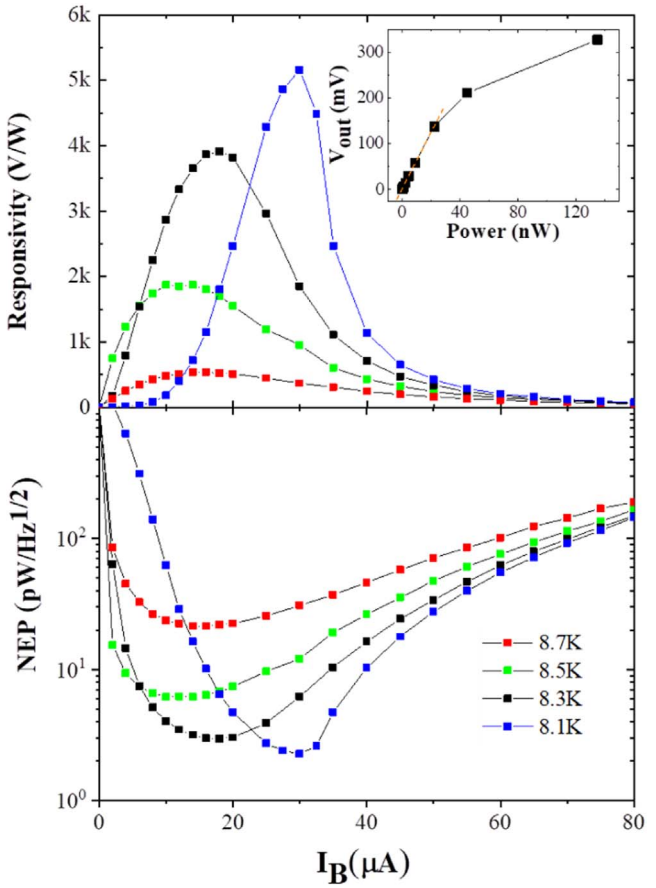

Figure 9. (a) HEB responsivity and (b) resulting NEP versus bias current for different bath temperatures. Inset: linearity of the device taken at $T = 8.3$ K and $I_B = 20$ μA.

amplifier (LNA, BW = 1 MHz−3 GHz), is recorded with an electronic spectrum analyser (ESA). Figure 8(b)) shows a family of IV characteristics of the HEB under test at different temperatures in a range between 8.1 and 8.7 K. The HEB has been operated as a direct detector, setting the operating temperature with a resistive heater located on the cold finger of the cryostat. The HEB can be polarized in each point of the characteristic as long as $\partial V/\partial I$ is continuous (to avoid instabilities in both detector biasing and response). In particular, the maximum responsivity, defined as $\text{Res} = \Delta V/P_{HEB}$, where ΔV is the change of the electronic signal amplitude at 10 MHz and $P_{HEB} = 22.7$ nW is the modulated optical power coupled to the chip, is obtained by polarizing the HEB with a current corresponding to the point of the characteristics where $\partial V/\partial I$ reaches its maximum [54, 55]. The responsivity reaches the largest value once the HEB switches in a stable resistive state of the IV characteristics (see figure 9(a)), in particular this is the region of the IV that can be modelled in terms of the expansion of a resistive hotspot. The detector NEP, i.e. the minimum incident power required to obtain a unit signal-to- noise ratio in a 1 Hz output bandwidth, is obtained as the ratio between V_n, the voltage noise fluctuation, measured by means of the ESA, and the responsivity Res (see figure 9(b)). The minimum NEP ≈ 2 $\text{pW}/\text{Hz}^{1/2}$ is reached at 8.1 K for $I_B = 30$ μA, where the responsivity has a maximum.

The detector shows a linear behaviour up to $P_{max} \sim 30$ nW of input signal corresponding to a dynamic range of 40 dB (inset in figure 9(a)) and a shot-noise power of 87.6 $\text{fW}/\text{Hz}^{1/2}$ [23]. This value is 15dB below the electronic NEP ≈ 3 $\text{pW}/\text{Hz}^{1/2}$ measured for the bias condition of $T = 8.3$ K and $I_b = 20$ μA. Differently from [23], where the HEB was operated as a mixer, the detector is not shot-noise limited for direct operation. For a silicon substrate, considering a 18 ps electron-photon interaction time, 65 ps escape time and a $c_p/c_e \approx 3.4$ (phonon to electron specific heat ratio) [56], the frequency dependence of the HEB response at $T \approx 8.1$ K, temperature close to T_c, can be calculated [57] resulting in a 3 dB cutoff frequency $f_c \approx 5.4$ GHz. This value is comparable with germanium detectors integrated on SOI waveguides that however do not suffer from a low saturation power. The advantage of NbN as photon conductive material resides in the technological compatibility with all the most common photonic platforms and SNSPD technology.

5. Conclusion

We have discussed performances of SNSPDs, array of SNSPDs and HEBs all integrated with photonic circuits for high sensitive optical detection. These NbN-based detectors, can detect light from the granular regime (single or few photons) up to weak continuous photon fluxes at wavelengths ranging from visible light up to mid-IR, NbN is one of the most used active material for the fabrication of SNSPDs and the technological compatibility with several photonic platforms has already been proved in both CMOS materials [13, 21, 58] and $LiNbO_3$ [59], to name a few. The possibility to integrate HEBs in photonic circuits, as linear detectors capable to measure with a low NEP high-intensity light signals (compared to the granular regime), together with single photon detectors opens the prospect for the on-chip generation and characterization of Schrödinger Kittens and, more generally, to realize fault tolerant universal quantum computers [60].

Acknowledgments

Some of the results of this paper have been obtained in the framework of a collaboration between the Institute for Photonics and Nanotehnology, IFN-CNR Rome, and the Andrea Fiore's group, Eindhoven University of Technology. We thank Prof A Fiore who provided during the ten-years long collaboration insight and expertise that greatly assisted the research. We would like to acknowledge also the project H2020-MSCA-IF-2017, No. 795923, SHAMROCK 'Superconductive MiR phOton Counter' for financing a part of this work.

ORCID iDs

Francesco Mattioli https://orcid.org/0000-0002-7242-3366

References

[1] Gisin N, Ribordy G, Tittel W and Zbinden H 2002 Quantum cryptography *Rev. Mod. Phys.* **74** 145–95
[2] Ladd T D *et al* 2010 Quantum computers *Nature* **464** 45–53
[3] Aspuru-Guzik A and Walther P 2012 Photonic quantum simulators *Nat. Phys.* **8** 285–91
[4] O'Brien J L, Furusawa A and Vučković J 2009 Photonic quantum technologies *Nat. Photon.* **3** 687–95
[5] Politi A, Cryan M J, Rarity J G, Yu S and O'Brien J L 2008 Silica on-silicon waveguide quantum circuits *Science* **320** 646–9
[6] Peruzzo A *et al* 2009 Quantum walks of correlated photons *Science* **329** 1500–3
[7] Spagnolo N *et al* 2014 Experimental validation of photonic boson sampling *Nat. Photon.* **8** 615–20
[8] Crespi A, Osellame R, Ramponi R, Giovannetti V, Fazio R, Sansoni L, Nicola D F, Sciarrino F and Mataloni P 2013 Anderson localization of entangled photons in an integrated quantum walk *Nat. Photon.* **7** 322–8
[9] Wang J *et al* 2015 Multidimensional quantum entanglement with large-scale integrated optics *Science* **360** 285–91
[10] Gol'tsman G *et al* 2001 Picosecond superconducting single-photon optical detector *Appl. Phys. Lett.* **79** 705
[11] Hadfield R 2009 Single-photon detectors for optical quantum information applications *Nat. Photon.* **3** 696–705
[12] Sprengers J P *et al* 2011 Waveguide superconducting single-photon detectors for integrated quantum photonic circuits *Appl. Phys. Lett.* **99** 181110
[13] Pernice W H P, Schuck C, Minaeva O, Li M, Goltsman G, Sergienko A V and Tang H X 2012 High-speed and high-efficiency travelling wave single-photon detectors embedded in nanophotonic circuits *Nat. Commun.* **3** 1325
[14] Schuck C, Pernice W H P and Tang H X 2013 Waveguide integrated lownoise NbTiN nanowire single-photon detectors with milli-Hz dark count rate *Sci. Rep.* **3** 1893
[15] Sahin D *et al* 2013 Waveguide photon-number-resolving detectors for quantum photonic integrated circuits *Appl. Phys. Lett.* **103** 111116
[16] Najafi F *et al* 2013 On-chip detection of non-classical light by scalable integration of single-photon detectors *Nat. Commun.* **6** 5873
[17] Reithmaier G, Kaniber M, Flassig F, Lichtmannecker S, Müller K, Andrejew A, Vuckovic J, Gross R and Finley J J 2015 On-chip generation, routing, and detection of resonance fluorescence *Nano Lett.* **15** 5208–13
[18] Rath P, Kahl O, Ferrari S, Sproll F, Lewes-Malandrakis G, Brink D, Ilin K, Siegel M, Nebel C and Pernice W 2015 Superconducting single photon detectors integrated with diamond nanophotonic circuits *Light: Sci. Appl.* **4** e338
[19] Vetter A *et al* 2016 Cavity enhanced and ultrafast superconducting single-photon detectors *Nano Lett.* **16** 7085–92
[20] Mattioli F, Zhou Z, Gaggero A, Gaudio R, Leoni R and Fiore A 2016 Photon-counting and analog operation of a 24-pixel photon number resolving detector based on superconducting nanowires *Opt. Express* **24** 9067–76
[21] Gaggero A, Martini F, Mattioli F, Chiarello F, Cernansky R, Politi A and Leoni R 2019 Amplitude-multiplexed readout of single photon detectors based on superconducting nanowires *Optica* **6** 823–8
[22] Wellstood F C, Urbina C and Clarke J 1994 Hot-electron effects in metals *Phys. Rev.* B **49** 5942
[23] Martini F *et al* Waveguide integrated hot electron bolometer for classical and quantum photonics to be published
[24] Gaggero A *et al* 2010 Nanowire superconducting single-photon detectors on GaAs for integrated quantum photonic applications *Appl. Phys. Lett.* **97** 151108
[25] Banerjee A, Heath R M, Morozov D, Hemakumara D, Nasti U, Thayne I and Hadfield R H 2018 Optical properties of refractory metal based thin films *Opt. Mater. Express* **8** 2072–88
[26] Il'in K S, Lindgren M, Currie M, Semenov A D, Gol'tsman G N, Sobolewski R, Cherednichenko S I and Gershenzon E M 2000 Picosecond hot-electron energy relaxation in NbN superconducting photodetectors *Appl. Phys. Lett.* **76** 2752
[27] Bulaevskii L N, Graf M J and Kogan V G 2012 Vortex-assisted photon counts and their magnetic field dependence in single-photon superconducting detectors *Phys. Rev.* B **85** 014505
[28] Vodolazov D Y 2014 Current dependence of the red boundary of superconducting single-photon detectors in the modified hot-spot model *Phys. Rev.* B **90** 054515
[29] Engel A, Lonsky J, Zhang X and Schilling A 2015 Detection mechanism in SNSPD: numerical results of a conceptually simple, yet powerful detection model *IEEE Trans. Appl. Supercond.* **25** 2200407

[30] Renema J J *et al* 2014 Experimental test of theories of the detection mechanism in a nanowire superconducting single photon detector *Phys. Rev. Lett.* **112** 117604
[31] Engel A, Schilling A, Il'in K and Siegel M 2012 Dependence of count rate on magnetic field in superconducting thin-film TaN single-photon detectors *Phys. Rev.* B **86** 140506(R)
[32] Renema1 J J *et al* 2015 The effect of magnetic field on the intrinsic detection efficiency of superconducting single-photon detectors *Appl. Phys. Lett.* **106** 092602
[33] Vodolazov D Y, Korneeva P, Semenov A V, Korneev A A and Goltsman G N 2015 Vortex-assisted mechanism of photon counting in a superconducting nanowire single-photon detector revealed by external magnetic field *Phys. Rev.* B **92** 104503
[34] Renema J J *et al* 2015 Position-dependent local detection efficiency in a nanowire superconducting single-photon detector *Nano Lett.* **15** 4541–5
[35] Kerman A J, Dauler E A, Yang J K W, Rosfjord M, Anant K V, Berggren K K, Gol'tsman G N and Voronov B M 2007 Constriction-limited detection efficiency of superconducting nanowire single-photon detectors *Appl. Phys. Lett.* **90** 101110
[36] Mattioli F, Leoni R, Gaggero A, Castellano M G, Carelli P, Marsili F and Fiore A 2007 Electrical characterization of superconducting single-photon detectors *J. Appl. Phys.* **101** 054302
[37] Achilles D, Silberhorn C, Sliwa C, Banaszek K and Walmsley I A 2003 Fiber-assisted detection with photon number resolution *Opt. Lett.* **28** 2387–9
[38] Banaszek K and Walmsley I A 2003 Photon counting with a loop detector *Opt. Lett.* **28** 52–4
[39] Dauler E A, Robinson B S, Kerman A J, Yang J K W, Rosfjord K M, Anant V, Voronov B, Gol'tsman G and Berggren K K 2007 Multi-element superconducting nanowire single-photon detector *IEEE Trans. Appl. Supercond.* **17** 279–84
[40] Divochiy A *et al* 2008 Superconducting nanowire photon-number-resolving detector at telecommunication wavelengths *Nat. Photon.* **2** 302–6
[41] Jahanmirinejad S and Fiore A 2012 Proposal for a superconducting photon number resolving detector with large dynamic range *Opt. Express* **20** 5017–28
[42] Jahanmirinejad S, Frucci G, Mattioli F, Sahin D, Gaggero A, Leoni R and Fiore A 2012 Photon-number resolving detector based on a series array of superconducting nanowires *Appl. Phys. Lett.* **101** 072602
[43] Zhou Z, Jahanmirinejad S, Mattioli F, Sahin D, Frucci G, Gaggero A, Leoni R and Fiore A 2014 Superconducting series nanowire detector counting up to twelve photons *Opt. Express* **22** 3475–89
[44] Zhu D, Zhao Q-Y, Choi H, Lu T-J, Dane A E, Englund D and Berggren K K 2018 A scalable multi-photon coincidence detector based on superconducting nanowires *Nat. Nanotechnol.* **13** 596–601
[45] Allman M S *et al* 2015 A near-infrared 64-pixel superconducting nanowire single photon detector array with integrated multiplexed readout *Appl. Phys. Lett.* **106** 192601
[46] Doerner S, Kuzmin A, Wuensch S, Charaev I, Boes F, Zwick T and Siegel M 2017 Frequency-multiplexed bias and readout of a 16-pixel superconducting nanowire single-photon detector array *Appl. Phys. Lett.* **111** 032603
[47] Hofherr M, Arndt M, Il'in K, Henrich D, Siegel M, Toussaint J, May T and Meyer H G 2013 Time-tagged multiplexing of serially biased superconducting nanowire single-photon detectors *IEEE Trans. Appl. Supercond.* **23** 2501205
[48] Zhao Q Y, Zhu D, Calandri N, Dane A E, McCaughan A N, Bellei F, Wang H Z, Santavicca D F and Berggren K K 2017 Single-photon imager based on a superconducting nanowire delay line *Nat. Photon.* **11** 247–51
[49] Gershenzon E M, Goltsman G N, Gogidze I G, Gusev Y P, Elantiev A I, Karasik B S and Semenov A D 1990 Millimeter and submillimeter range mixer based on electronic heating of superconducting films in the resistive state *Superconductivity* **3** 1582–97
[50] Lobanov Y *et al* 2014 Heterodyne detection at near-infrared wavelengths with a superconducting NbN hot-electron bolometer mixer *Opt. Lett.* **39** 1429–32
[51] Ren Y, Zhang D, Wang Z, Zhou K, Zhong J, Liu D, Miao W, Zhang W and Shi S 2020 Quantum cascade laser based, fiber coupled demultiplexed mid-infrared local oscillator for cryogenic applications *Appl. Phys. Lett.* **116** 131108
[52] Seliverstov S, Maslennikov S, Ryabchun S, Finkel M, Klapwijk T M, Kaurova N, Vachtomin Y, Smirnov K, Voronov B and Goltsman G 2015 Fast and sensitive terahertz direct detector based on superconducting antenna-coupled hot electron bolometer *IEEE Trans. Appl. Supercond.* **25** 1–42300304
[53] Cibella S, Carelli P, Castellano M G, Chiarello F, Gaggero A, Giovine E, Scalari G, Torrioli G and Leoni R 2017 A metamaterial-coupled hot-electron-bolometer working at THz frequencies *Terahertz, RF, Millimeter, and Submillimeter-Wave Technology and Applications X* 10103 ed L P Sadwick and T Yang (SPIE) 101031M
[54] Shurakov A *et al* 2016 Superconducting hot electron bolometer: from the discovery of hot electron phenomena to practical application *Supercond. Sci. Technol.* **29** 023001
[55] Klapwijk T M and Semenov A V 2017 Engineering physics of superconducting hot-electron bolometer mixers *IEEE Trans. Terahertz Sci. Technol.* **6** 627
[56] Tretyakov I, Ryabchun S, Finkel M, Maslennikova A, Kaurova N, Lobastova A, Voronov B and Gol'tsman G 2011 Low noise and wide bandwidth of NbN hot-electron bolometer mixers *Appl. Phys. Lett.* **98** 033507
[57] Perrin N and Vanneste C 1983 Response of superconducting films to a periodic optical irradiation *Phys. Rev.* B **28** 5150–9
[58] Martini F, Gaggero A, Mattioli F and Leoni R 2019 Single photon detection with superconducting nanowires on crystalline silicon carbide *Opt. Express* **27** 29669
[59] Al Sayem A, Cheng R, Wang S and Tang H X 2020 Lithium-niobate-on-insulator waveguide-integrated superconducting nanowire single-photon detectors *Appl. Phys. Lett.* **116** 151102
[60] Alexander R N, Yokoyama S, Furusawa A and Menicucci N C 2018 Universal quantum computation with temporal-mode bilayer square lattices *Phys. Rev.* A **97** 32302